Silicone Resin Derived Larnite/C Scaffolds via 3D Printing for Potential Tumor Therapy and Bone Regeneration

Shengyang Fu, Haoran Hu, Jiajie Chen, Yufang Zhu, Shichang Zhao

PII: S1385-8947(19)32338-1
DOI: https://doi.org/10.1016/j.cej.2019.122928
Reference: CEJ 122928

To appear in: *Chemical Engineering Journal*

Received Date: 5 May 2019
Revised Date: 9 September 2019
Accepted Date: 21 September 2019

Please cite this article as: S. Fu, H. Hu, J. Chen, Y. Zhu, S. Zhao, Silicone Resin Derived Larnite/C Scaffolds via 3D Printing for Potential Tumor Therapy and Bone Regeneration, *Chemical Engineering Journal* (2019), doi: https://doi.org/10.1016/j.cej.2019.122928

Silicone Resin Derived Larnite/C Scaffolds via 3D Printing for Potential Tumor Therapy and Bone Regeneration

Shengyang Fu[a,b,1], Haoran Hu[c,1], Jiajie Chen[a], Yufang Zhu[a,b]*, Shichang Zhao[c]*

[a] School of Materials Science and Engineering, University of Shanghai for Science and Technology, 516 Jungong Road, Shanghai 200093, China.

[b] Hubei Key Laboratory of Processing and Application of Catalytic Materials, College of Chemical Engineering, Huanggang Normal University, Huanggang City, Hubei Province, 438000, China.

[c] Department of Orthopedics, Shanghai Jiao Tong University Affiliated Sixth People's Hospital, Shanghai Jiaotong University, No.600 Yishan Road, Shanghai 200233, China.

*Corresponding authors:

Prof. Yufang Zhu: Tel: +86-21-55271663; Email: zjf2412@163.com

Dr. Shichang Zhao: Tel: +86-21-64369181; Email: zhaoshichang0404@163.com

[1] The first two authors contributed equally to this work.

Abstract：

Three dimensional (3D) printing has been used to fabricate bioceramic scaffolds for treating the tumor-related defects in recent years, but the fabrication process and the introduction of anti-tumor agents are still challenging. In this study, porous free carbon-embedding larnite (larnite/C) scaffolds have been successfully fabricated by 3D printing of the silicone resin loaded with $CaCO_3$ filler and high temperature treatment under an inert atmosphere. The fabricated larnite/C scaffolds had uniform interconnected macropores (ca. 400 μm), and exhibited excellent photothermal effect, which was able to kill human osteosarcoma cells (MNNG/HOS) and inhibit the tumor growth in nude mice. Moreover, the larnite/C scaffolds could stimulate the expression of osteogenesis-related gene (ALP, OCN and Runx-2) in rat bone mesenchymal stem cells (rBMSCs), and also promoted new bone formation in critical-sized rat calvarial defects. Therefore, the combination of 3D printing with polymer-derived ceramics strategy could fabricate multifunctional bioceramic scaffolds, which would be promising for potential application in treating tumor-related bone defects.

Keywords: Scaffolds; Polymer-derived bioceramics; 3D printing; Tumor therapy; Bone regeneration.

1. Introduction

In tissue engineering, porous scaffolds can not only act as a temporary support for cells at initial stage, but also contribute the angiogenesis ability, cell migration, and nutrient transport and metabolism abilities. Therefore, the scaffolds are widely applied for tissue repair and/or regeneration, such as bone, skin, tooth, tendon and ligament [1]. Bioactive scaffolds with interconnected pores and proper pore size are promising for treating bone defects in bone tissue engineering, because the scaffold structure facilitates material degradation, angiogenesis, cell migration, nutrient transport and metabolism in defects [2, 3]. Generally, pore forming methods includes polyurethane (PU) foam templating, polymethyl methacrylate (PMMA) templating, gas foaming, freeze drying, etc. However, it is not easy to control pore size and morphology precisely by these methods, and a controllable ability for making pores is necessary. Nowadays, three-dimensional (3D) printing technique has been significantly developed to fabricate porous scaffolds for bone regeneration due to its high efficiency and precision, through computer-assisted design (CAD)/computer-aided manufacturing (CAM). A variety of bioactive ceramics for bone tissue engineering have been successfully fabricated by 3D printing, such as hydroxyapatite (HA) [4, 5], bioactive glasses (BG) [6, 7], calcium phosphate [8-11] and silicate-based bioceramics [12]. However, these bioactive materials could not satisfy the treatments of bone defects caused by bone tumor surgery, because the proliferation of residual tumor cells inevitably leads to tumor recurrence. It is worthy to design and fabricate a type of bioactive scaffolds for the tumor-caused bone defects, which not only

stimulates bone regeneration to repair the large defects, but also owns the ability to kill the residual tumor cells at the same time.

Photothermal therapy (PTT) employs the photothermal agents to generate heat under near-infrared light irradiation to ablate tumor cells. Compared to the traditional tumor therapies, such as chemotherapy and radiotherapy, PTT is a targeted and local therapy with minimal invasiveness and high efficiency [13-17]. In recent years, PTT has been rapidly developed, and many photothermal agents have been adopted, such as organic particles [16, 18], gold nanoparticles [19], molybdenum sulfide (MoS_2) [20], graphene oxide (GO) [17, 21], carbon dots (CDs) [22-24], $CuFeSe_2$ [25], etc. However, most of photothermal agents were used in the form of nanoparticles, for treating such breast cancer, colon cancer, etc. For instance, Yao et al.[24] constructed a multifunctional platform composed of graphene quantum dots and magnetic mesoporous silica nanoparticles, which could inhibit breast cancer 4T1 cells owing to synergistic therapy with photothermal, magnetic hyperthermia and chemotherapy. Zheng et al.[22] synthesized multifunctional carbon dots with photothermal effect and fluorescence imaging, which was able to kill HepG2 cells under infrared light irradiation due to high photothermal conversion efficiency. Interestingly, Ma et al.[21] designed graphene oxide (GO)-modified β-tricalcium phosphate (β-TCP) scaffolds (GO-β-TCP) for bone regeneration and tumor therapy. In this study, β-TCP scaffolds were prepared by 3D printing of β-TCP/PVA inks to form green scaffolds and following a sintering process. The GO-β-TCP scaffolds were obtained through the soaking of β-TCP scaffolds in GO solution. Yang et al.[26] reported a black-phosphorus modified BG

scaffolds, which showed that black phosphorus acted as photothermal agents for cancer therapy and initiators for guided bone generation. These functionalized scaffolds have the ability to kill tumor cells and stimulate new bone formation. However, the fabrication methods are too complicated, which involves in preparation of bioceramic powders, 3D printing for the fabrication of green scaffolds, sintering for densification and modification with photothermal agents. Furthermore, the modification processes including hydrothermal and solvothermal treatments may destroy the scaffolds to some extent.

To simplify the fabrication processes, polymer-derived ceramics (PDCs) strategy combined with 3D printing technique would be optimal. One of the most important advantages is the possibility of combining the shaping and synthesis of ceramics [27]. Different bioceramics such as wollastonite ($CaSiO_3$), hardystonite ($Ca_2ZnSi_2O_7$), akermanite ($Ca_2MgSi_2O_7$) [28-30] can be fabricated from organosilicon polymers loaded with active fillers during a polymer-to-ceramic conversion. For example, Zocca et al.[28] fabricated a porous hardystonite ($Ca_2ZnSi_2O_7$) bioceramic scaffolds by direct ink writing, and a printable paste was prepared by mixing ZnO and $CaCO_3$ active fillers with polysiloxane. Elsayed et al.[29] fabricated wollastonite/diopside composite scaffolds by direct ink writing, which also derived from the polysiloxane with $CaCO_3$ and $Mg(OH)_2$ active fillers. Importantly, it cannot be ignored the existence of carbon atoms in organosilicon polymers, which could be pyrolyzed into free carbon in the matrix during ceramic transformation under an inert atmosphere, and the pyrolyzed free carbon plays an important role in the physicochemical properties of ceramics. For

instance, Fiocco et al. [31] fabricated wollastonite-diopside-carbon composite foams, which was derived from a silicone resin with inorganic fillers. The free carbons were formed due to the pyrolysis of silicone resin under a nitrogen atmosphere, which decreased the amounts of cracks in ceramic foam. Elsayed et al. [32] designed a silica-carbon-calcite scaffold by direct ink writing, and the existence of free carbons in composite scaffolds improved the mechanical strength. Moreover, free carbon has emerged an enhanced capacity for osteogenic differentiation [33], and a potential photothermal effect [23]. Therefore, it encourages us to fabricate multifunctional bioceramic scaffolds with photothermal effect and bone regeneration ability by the combination of PDCs strategy with 3D printing. To the best of our knowledge, there are no reports describing such novel and facial strategy to fabricate bioceramic scaffolds for potential bone tumor therapy and bone regeneration.

In this study, polysilsesquioxane silicone and $CaCO_3$ active filler powders were homogeneously mixed for 3D printing, and then the green scaffolds underwent a ceramic transformation under an argon atmosphere to form free carbon-embedding larnite (larnite/C) scaffolds (Scheme 1). Larnite is one of bioactive ceramics that has excellent apatite formation ability and promotion to osteogenic gene expression [34-37]. Carbon exhibits good biocompatibility, optical properties and low toxicity [38-41]. Meanwhile, free carbon is able to absorb near-infrared light and have a high photothermal conversion efficiency to kill tumor cells. By taking the advantages of the photothermal effect of free carbon and the bone regeneration ability of larnite, the larnite/C composite scaffolds have the ability to inhibit tumor growth and promote

new bone formation, which show great potential for the treatment of malignant bone tumor-induced defects (Scheme. 1).

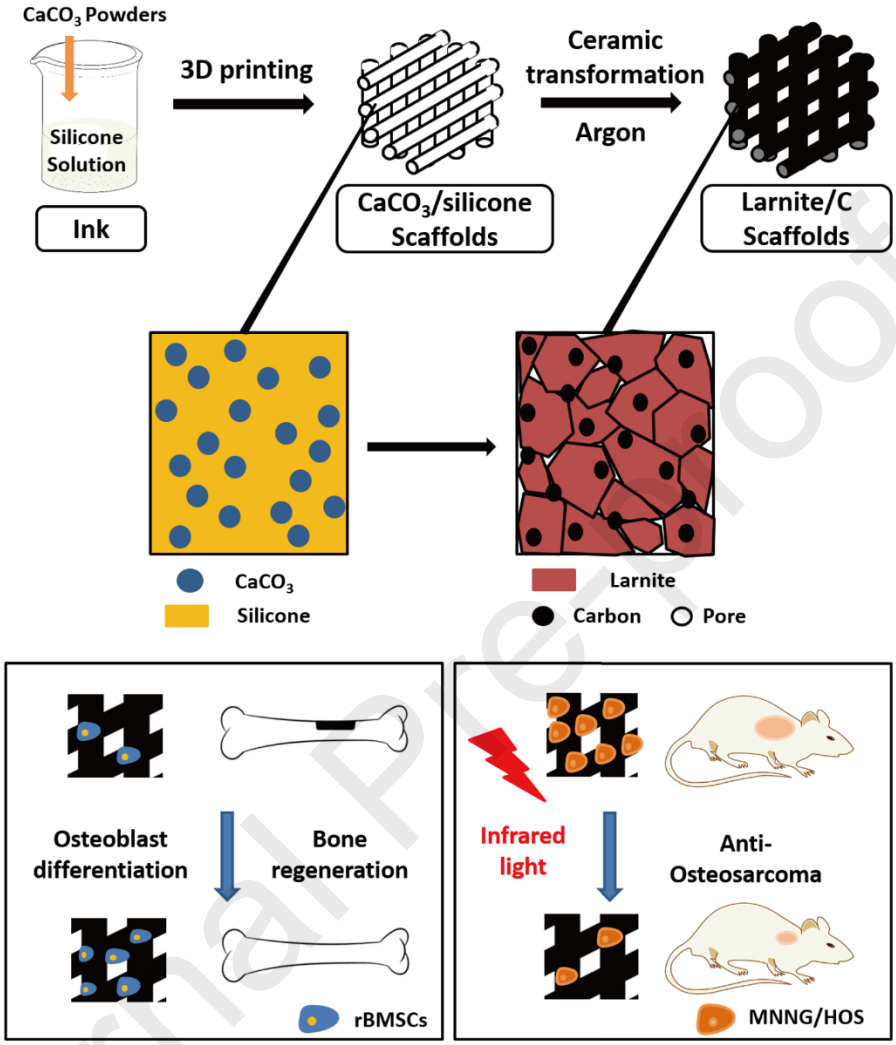

Scheme. 1 Schematic illustration for the fabrication process of the larnite/C scaffolds and their functions for tumor therapy and bone regeneration.

2. Experiment Section

2.1 Materials

A commercial silicone resin (polysilsesquioxane, Silres®MK) was purchased from WackerChemie (Munich, Germany). Calcium carbonate ($CaCO_3$, ≥99.0%), calcium

nitrate tetrahydrate ($Ca(NO_3)_2{\cdot}4H_2O$, ≥99.0%), tetraethyl orthosilicate ($Si(OC_2H_5)_4$, TEOS, 98%), nitric acid (HNO_3, ≥65%), trichloromethane ($CHCl_3$) and isopropyl alcohol were purchased from Sinopharm Chemical Reagent Co. Ltd (Shanghai, China). Polycaprolactone (PCL, Mn=70,000-90,000) were purchased from Sigma-Aldrich (USA). All chemicals were used without further purification.

2.2 Fabrication of scaffolds by 3D printing and ceramic transformation

The silicone resin-derived larnite (larnite/C) scaffolds were fabricated by 3D printing as follows. Firstly, an injectable paste was prepared by mixing the $CaCO_3$ powders (≤38 μm) with silicone resin in isopropyl alcohol (0.4 ml per gram of silicone resin), and the Ca/Si molar ratio was 2:1. Subsequently, the injectable ink was introduced into a plastic injection cartridge which was fixed onto the 4th 3D Bioplotter™ (EnvisionTEC GmbH, Germany). Next, a cylinder model (d= 10 mm) was loaded on the Bioplotter software and green scaffolds were printed through the extrusion of the ink as a fiber with a diameter of 400 μm, 600 μm and 800 μm, and the angle of the successive layers was 60° [1, 2]. The designed structure was formed by the extrusion of printing ink layer-by-layer, and the obtained green scaffolds were dried at 37 ^{o}C. Finally, green scaffolds were treated at different temperatures (1000 ^{o}C, 1100 ^{o}C, 1200 ^{o}C) for 3 hours with 2 ^{o}C/min heating rate in argon atmosphere. The final scaffolds were named as larnite/C-1, larnite/C-2 and larnite/C-3, respectively.

As a control group, pure larnite powders were synthesized from $Ca(NO_3)_2{\cdot}4H_2O$ and TEOS by a sol-gel method [42, 43]. Typically, 20.83 ml HNO_3, 17.36 g $Ca(NO_3)_2{\cdot}4H_2O$ and 8.5 g TEOS were added into 130 ml deionized water, and the

mixture was stirred at 38 °C in water bath for 24 h. The resulting sol was dried at 100 °C for 24 h, and the as-synthesized gel was calcined at 800 °C with a 5 °C/min heating rate for 3 h. After grinding and sieving, pure larnite powders with particle size less than 38 μm were obtained. To fabricate pure larnite scaffolds by 3D printing, pure larnite powders were mixed into the PCL solution in trichloromethane to form a printable ink. Here, PCL acts as a binder with 5 wt% in the ink. The 3D printing process was the same as the above processes for the silicone resin-derived larnite scaffolds. After 3D printing, the scaffolds were sintered at 1000 °C in air for 3 h with a 2 °C/min heating rate.

2.3 Characterization of silicone resin and scaffolds

To prove if free carbons were in the pyrolyzed silicone resin, silicone resin (SR) was pyrolyzed at 1000 °C in air and argon atmospheres, which named as SR-Air and SR-Ar, respectively. Thermogravimetric analysis (TGA) was performed on STA 449 F3 thermal analyzer in air atmosphere with a flow rate of 20 ml/min and a heating rate of 10 °C/min, and mass spectrum was carried out from QMS 430D mass spectrometer with the same condition (Netzsch, Germany). XPS was tested with an ESCALAB 250 X-ray photoelectron spectrometer using Al Kα (hν = 1486.6 eV) radiation. The XRD patterns were obtained on a D8 ADVANCE powder diffractometer using Cu Kα1 radiation (1.5405 Å). Scanning electron microscopy (SEM) was carried out using an FEI Quanta 450 field emission scanning electron microscope. Raman spectra was performed on the Raman spectroscopy (RamanStationTM 400/400F, PE, USA) with a semiconductor laser (532 nm). The compressive strength of the scaffolds was tested by a static materials testing machine (2.5 kN) (Zwick Roell, Ulm, Germany) at a

crosshead speed of 0.5 mm/min.

2.4 Photothermal effect of the scaffolds

The 808 nm laser generator (Shanghai Connect Fiber Optics Company, China) (Fig. S1) mainly consists of laser diode controller, laser transmitter and collimator. The wavelength is approximate 808 nm, and its power density could be regulated by current intensity (linear relationship) on the screen of laser diode controller. The 808 nm laser is generated from laser transmitter with a collimator (area: 0.25 cm^2).

To explore photothermal effect of the scaffolds, the scaffolds were placed in a 24-well culture plate. Then, the near-infrared (NIR) light beam was focused on the scaffolds at a power density of 0.5 W/cm^2, 0.75 W/cm^2 or 1 W/cm^2, which was generated by an 808 nm high power multimode pump laser. To evaluate the photothermal effect of the scaffolds in wet condition, the scaffolds were put into plate with 1 ml PBS solution, then irradiated by 808 nm laser. To evaluate the photothermal effect of the scaffolds in nude mice, the scaffolds were implanted in nude mice, and the nude mice were irradiated with 808 nm laser (0.75 W/cm^2 and 1 W/cm^2) for 10 min, of which the real temperature changes were monitored by imaging instrument. The corresponding thermal images with the temperature changes were recorded on an infrared thermal imaging instrument (FLIRTM A325SC camera, USA).

2.5 In vitro killing bone-tumor cells by photothermal effect

Osteosarcoma cells (MNNG/HOS) were cultured in MEM medium supplemented with 10 % fetal bovine serum (FBS) under 5 % CO_2 at 37 ^oC. In order to test cell viability, 1.0×10^4 of MNNG cells were cultured in 48-well plate for 24 h. The larnite and

larnite/C-3 scaffolds were put into the plate. Then, these scaffolds were irradiated by 808 nm laser with different power density of 0 W/cm^2, 0.5 W/cm^2, 0.75 W/cm^2, and 1 W/cm^2, respectively. Finally, all the scaffolds were taken out and the MNNG cells on the slices were stained with LIVE/DEAD™ Viability/Cytotoxicity Kit (Thermo Fisher, USA) to differentiate dead tumor cells and live tumor cells.

2.6 In vivo therapy of bone tumor tissue by photothermal effect

All animal surgical procedures were approved by the Animal Care and Experiment Committee of Shanghai Jiao Tong University Affiliated Sixth People's Hospital. MNNG tumor cells (5.0×10^4) were injected into the back of nude mice (4 weeks' old). When the tumor volume came to about 200 mm^3, the mice were divided into four groups randomly. Then, the larnite and larnite/C-3 scaffolds were implanted into the center of tumor issue (larnite/C-3 scaffolds with or without NIR irradiation treatments, larnite scaffolds with or without NIR irradiation treatments). For NIR irradiation treatments, the power density of 0.75 W/cm^2 for 10 min was employed every two days. The first day treatment was regarded as day 0, and the treatment continued for 14 days. The tumor length and width in each group were measured by vernier caliper for each four day. At day 14, the real temperature changing were monitored by imaging instrument as well. Finally, the nude mice were sacrificed. The tumor tissues were obtained, which fixed with 4 % neutral buffered formalin and embedded in paraffin, sliced, stained with Hematoxylin eosin (H&E), and they were evaluated with a light microscopy (Leica, Germany). These tissue slices were used and the vision were measured randomly.

2.7 In vitro osteogenic activity

The rat bone mesenchymal stem cells (rBMSCs) were harvested from the femur of 2-week-old S-D rats. For initial adhesion assay, larnite and larnite/C-3 scaffolds were seeded with 10^5 rBMSCs in 24-well culture plates and incubated in DMEM supplemented with 10% FCS at 37℃ in a humidified atmosphere of 5% CO_2. After 3 days, samples were washed with PBS for three times, then 4% paraformaldehyde was added to fix the cells remained on the scaffolds for 30 min at room temperature. Subsequently, cell nuclei and cytoskeleton of rBMSCs on scaffolds were then stained with DAPI and rhodamine phalloidin, respectively. The proliferation of the rBMSCs on the scaffolds was assessed using Cell Counting Kit (CCK-8) assay (Dojindo, Japan). Briefly, rBMSCs were cultured on the scaffolds (n = 3) using the procedure described above at an initial density of 10^4 cells per scaffold for 1, 3 and 7 days. Briefly, 450 µl of culture medium and 50 µl of CCK-8 solution were added to each well. An aliquot of 100 µl of each group was transferred to another 96-well plate and absorbance at 450 nm was measured with a microplate reader (Bio-Rad 680; Bio-Rad, Hercules, CA, USA). To determine ALP activity of osteoblasts on the scaffolds, 1×10^4 rBMSCs were seeded on each scaffold and cultured in a 24-well plate for 7 and 14 days, respectively. The ALP activity was estimated by the p-nitrophenyl-phosphate (pNPP) method. At the predetermined time point, culture medium was removed and washed with PBS three times, followed by washing once in cold 50 mM Tris-buffer, and then cells were lysed in 0.1% Triton X-100. Then pNPP (Beyotime Biotechnology, China) was added for 60 min at 37°C. Finally, 1 M NaOH solution was added to quench the chromogenic reaction. The results were obtained by measuring the absorbance at 405 nm with a

microplate reader (Bio-Rad680, USA). In addition, the rBMSCs cultured on the scaffolds in the 24-well transwell plate were fixed with glutaraldehyde on day 7 and 14, then incubated BCIP/NBT kit (Beyotime Biotechnology, China) and alizarin red S (Cyagen, USA) for 10 min repesctively. Finally, photos were taken with a camera (Canon, Japan) and a microscope (Leica, Germany).

The relative expression of ALP, osteocalcin (OCN) and runt-related transcription factor 2 (Runx-2) were measured by quantitative real-time PCR. Briefly, rBMSCs seeded at a density of 2×10^4 on each scaffold were cultured for 7 or 14 days and harvested using Trizol Reagent to obtain RNA. The acquired DNA was reverse-transcribed into complementary DNA (cDNA) using Revert-Aid First Strand cDNA Synthesis Kit (Thermo) and the qRT-PCR analysis was performed on an ABI Prism 7300 Thermal Cycler (Applied Biosystems, Australia) using SYBR Green detection reagent. The relative expression of the osteogenic genes was normalized according to the housekeeping gene GAPDH. All samples were tested intriplicate and independent experiments were performed. The mean cycle threshold (Ct) value of each target gene was normalized against the Ct value of GAPDH. The relative expression was calculated using the following formula: $2^{(-\text{normalized average Ct})}\times100$.

2.8 In vivo bone regeneration activity

Twenty mature male Sprague Dawley (SD) rats (12 weeks old, mean body weight: 250-300 g) were used. In the surgical procedures, the rats were anesthetized by intraperitoneal injection and calvarium was exposed by blunt dissection. Then, two 5 mm diameter calvarial defects were created by a dental trephine. The rats were

divided into 3 groups randomly. One group was the control group without the implantation, and other two groups were implanted with the larnite and larnite/C-3 scaffolds. After 8 weeks' culture, the rats were sacrificed, of which crania were fixed in a 4% paraformaldehyde solution buffered with 0.1 M phosphate solution (pH = 7.2).

To evaluate new bone formation within the defect region, all the harvested specimens were examined using a micro-CT system (Skyscan, Belgium). Briefly, the specimens were scanned with a thickness of 18 μm per slice in medium-resolution mode. After 3D reconstruction, bone mineral density (BMD) and bone volume fraction (BV/TV) were automatically determined using the auxiliary software (Skyscan Software), which were used to evaluate new bone formation.

In addition, the specimens were dehydrated through ascending concentrations of alcohol from 70% to 100%, and then embedded in polymethylmethacrylate (PMMA). After hardening, the longitudinal sections of the crania were cut into 150-200 μm thick slices using a microtome (Leica Microsystems, Wetzlar, Germany). Next, the sections with fluorescent labeling were observed by confocal laser scanning microscopy (CLSM, Leica, Germany). The excitation/emission wavelengths of the chelating fluorochromes used were 405/560–590 nm (Tetracycline, yellow), 543/580–670 nm (Alizarin red, red) and 488/500–550 nm (Calcein, green).

In H&E and Masson's trichrome staining, the sections were stained with Hematoxylin-Eosin and Masson's Trichrome Stain Kit (Solarbio, China), then examined in an optical microscope (Leica, Germany). In immunohistochemical staining, sections incubated with OCN and Runx-2 primary antibody at 4 ^{o}C overnight and incubated with

secondary antibody for 1 h, and the diaminobenzidine (Dako, Danmark) were used to develop the color reaction. Finally, the sections were examined under a light microscope (Leica, Germany).

2.9 Statistical analysis

Three separate experiments were carried out to collect the data, and then the data was expressed as means ± standard deviation. The level of significance was determined by the one-way ANOVA and Student-Newman-Keuls post hoc tests, and P values were considered to be significant. (*P < 0.05)

3. Results and Discussion

Carbon atoms commonly exist in the backbone and side groups of silicone resin, and the pyrolyzed free carbons are important components in silicone resin-derived ceramics [44]. However, the content of free carbon in the silicone resin-derived ceramics is greatly affected by the treatment atmosphere. Fig. 1 showed the analysis for the pyrolyzed silicone resin at 1000^{o}C under air and argon atmospheres. It could be observed that the pyrolyzed silicone resin under air atmosphere was white, while that under argon atmosphere was black (Fig. 1(a), (b)), which suggested free carbons might be formed in the pyrolyzed silicone resin under argon atmosphere. Fig. 1(c) and 1(d) showed the TGA curves coupled with mass spectra (z= 44) in the air flow for the pyrolyzed silicone resin under air and argon atmospheres. The pyrolyzed silicone resin under air atmosphere had only one weight loss before 300 ^{o}C, and no z=44 signals were observed on mass spectrum, indicating little free carbons could be formed

during the pyrolysis of silicone resin under air atmosphere. Instead, the pyrolyzed silicone resin under argon atmosphere exhibited two weight losses before 300 ^{o}C and after 600 ^{o}C, and two z=44 signals were recorded on mass spectrum correspondingly, which suggested that CO_2 was produced due to the reaction between free carbons and O_2 in air flow. That is to say, free carbons had been formed in the pyrolyzed silicone resin under argon atmosphere. In addition, XPS analysis also qualitatively confirmed more free carbons in the pyrolyzed silicone resin under argon atmosphere (Fig. S2). Therefore, the results indicated that silicone resin with $CaCO_3$ active filler was possible to form the free carbon-embedding larnite after the pyrolysis under argon atmosphere. Silicone resin as a common preceramic polymer has been broadly applied for fabricating silicon-based bioceramics [45, 46]. The backbone Si-O and some side chains Si-C of silicone resin could be destroyed at high temperature, which transform into a silica residues in air atmosphere, and a SiOC (including Si-C bond and free carbons) residues in non-oxidative atmosphere, respectively, because most free carbons are easily burned out with oxygen. On the other hand, the perfect rheological property of silicone resin simplifies the shape process of bioceramics. Hence, the combination of silicone resin-derived strategy and 3D printing provides a facial and efficient method for fabricating silicate-based bioceramics with a complex structure.

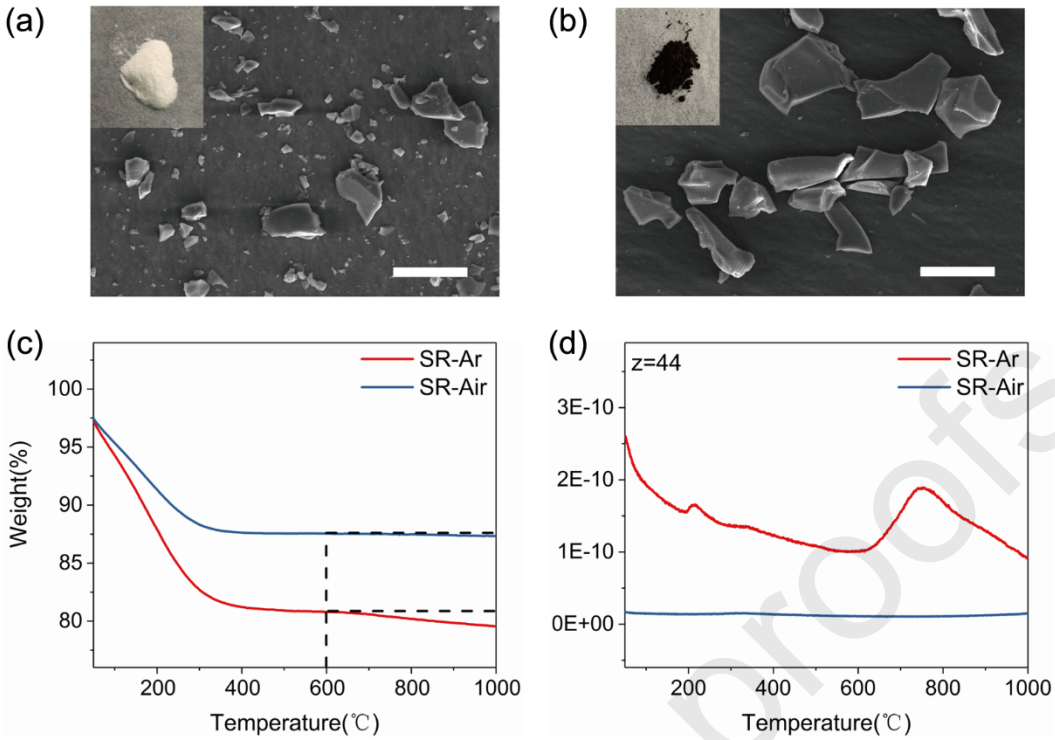

Fig. 1 The pyrolysis for the pyrolyzed silicone resin at 1000 °C under air and argon atmospheres. SEM images and photographs of the pyrolyzed silicone resins treated at 1000 °C under (a) air and (b) argon (scale bar: 50 μm). (c) TGA curves and (d) the corresponding mass spectra with z= 44 in the air flow for the pyrolyzed silicone resin under air and argon atmospheres.

To fabricate porous larnite/C scaffolds, a printable ink was prepared by mixing the silicone resin and $CaCO_3$ powders in isopropyl alcohol with a stoichiometric Ca/Si ratio 2:1. The larnite/C scaffolds were obtained by 3D printing and treated at 1000-1200 °C under argon atmosphere, and the scaffolds treated at 1000 °C, 1100 °C and 1200 °C were named as the larnite/C-1, larnite/C-2 and larnite/C-3 scaffolds, respectively. As a control, the pure larnite scaffolds were fabricated by 3D printing of the sol-gel larnite powders and sintering. The diffraction peaks of larnite phase (JCPDS

card 33-0302) were observed for each type of scaffolds over 1000 °C (Fig. 2(a)), which indicated the absolute conversion to larnite ceramics through the reaction between $CaCO_3$ and silicone resin during high temperature treatment over 1000 °C. Fig. 2(b) showed SEM images of the 3D printed larnite and larnite/C scaffolds. The regular interconnected macropores (ca. 400 μm) of the scaffolds were maintained after high temperature treatment at 1000, 1100 and 1200 °C. Compared to the white larnite scaffolds, the silicone resin-derived larnite/C scaffolds exhibited grey and black (Fig. S3), suggesting that free carbons were formed in the larnite/C scaffolds due to the pyrolysis of silicone resin under argon atmosphere. During high temperature treatment in argon, silicone resin first transferred into SiOC (including Si-C bond and free carbons), and then SiOC reacted with CaO derived from the decomposition of $CaCO_3$ to form larnite, while free carbons maintained to obtain larnite/C scaffolds. For silicone resin-derived larnite/C scaffolds, the compressive strength was enhanced from 1.8 ± 0.2 MPa to 4.8 ± 0.5 MPa by increasing the heat treatment temperature (Fig. S4), which might be attributed to the higher crystallinity and density. Raman spectra showed the typical bands of graphitic-like carbon at 1334 cm^{-1} (D band) and 1607 cm^{-1} (G band) in the larnite/C scaffolds, but the larnite scaffolds did not have obvious characteristic bands of carbon. The I_D/I_G ratios of the larnite/C-1, larnite/C-2 and larnite/C-3 scaffolds are 1.45, 1.03 and 1.01 respectively, indicating the graphitic degree of free carbons increased due to the higher kinetic energy provided by the increase of heat treatment temperature. Furthermore, the free carbon contents for each type of scaffolds were estimated by EDS analysis, and the results showed that

they were 1.41 w%, 5.57 w%, 6.57 w% and 7.04 w% for the larnite, larnite/C-1, larnite/C-2 and larnite/C-3 scaffolds, respectively. Fig. 2(d) showed the element mapping of the fracture surface for the larnite/C-3 scaffolds, which confirmed the free carbons were homogeneously distributed in the scaffolds. Therefore, the 3D printed green scaffolds composed of silicone resin and $CaCO_3$ filler could convert to the free carbon-embedding larnite scaffolds. Significantly, many other forming methods can also achieve adding free carbons into the scaffolds. However, in this study, the introduction of free carbons into scaffolds is using polymer-derived ceramics strategy (PDCs), instead of shaping method. Without PDCs strategy, the fabricating process would be tedious, containing bioceramic powders preparation, free carbon preparation, physical mix, shaping and sintering. Hence, the combination of 3D printing and PDCs is a simple and efficient method for fabricating larnite/C scaffolds, and the scaffolds have potential functions for photothermal therapy and bone regeneration.

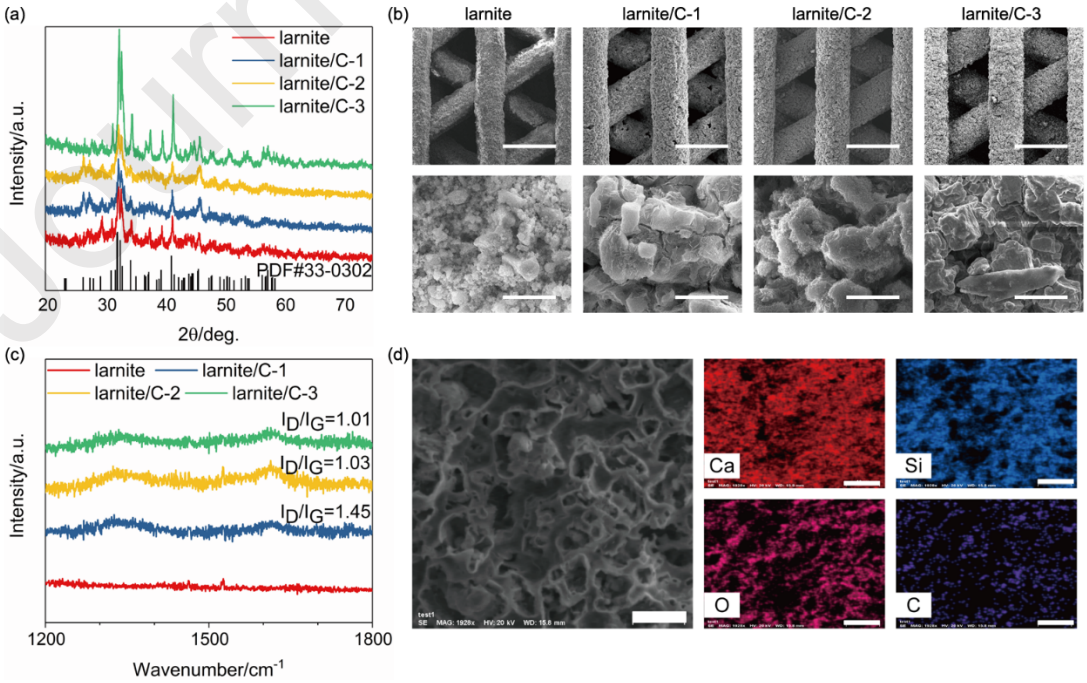

Fig. 2 Structural and compositional characterizations of the larnite/C scaffolds. (a) XRD patterns, (b) SEM images (scale bar: above, 500 μm; below, 20 μm) and (c) Raman spectra of the larnite and larnite/C scaffolds. (d) SEM image and element mappings for the fracture surface of the larnite/C-3 scaffolds (scale bar: 10 μm).

To verify the photothermal therapy function of the larnite/C scaffolds, the in vitro and in vivo photothermal performance of the larnite/C scaffolds were systematically evaluated. Fig. 3 showed the in vitro photothermal effect of the larnite and larnite/C scaffolds irradiated at a power intensity of 0.75 W/cm^2 for 5 min. It could be observed that the larnite scaffolds had poor photothermal effect. The surface temperature of the scaffolds only increased from 28 ^{o}C to 35 ^{o}C, and the photothermal effect further decreased when the larnite scaffolds were soaked in PBS. However, the larnite/C scaffolds exhibited an excellent photothermal effect. The surface temperatures on the larnite/C-1, larnite/C-2 and larnite/C-3 scaffolds increased to 61 ^{o}C, 63 ^{o}C and 61 ^{o}C, respectively. Furthermore, when the larnite/C scaffolds were soaked in PBS, the temperature for the larnite/C-1, larnite/C-2 and larnite/C-3 scaffolds still can respectively reach to 46 ^{o}C, 48 ^{o}C and 48 ^{o}C due to the generated heat from the scaffolds transferred to the PBS medium, which meet the temperature range for hyperthermia therapy. Here, the larnite/C scaffolds treated at 1000 - 1200 ^{o}C showed very close photothermal effect, which might be attributed to the similar free carbon contents in the scaffolds, and the little difference on graphitic degree of free carbons did not affect obviously. Interestingly, the photothermal effect of the scaffolds could

be regulated to some extent by controlling the NIR light power intensity and different scaffold structure (Fig. S5 and S6). The photothermal effect of the scaffolds with a lower porosity (spacing of adjacent fibers: 400 μm) was better than that of 600 μm and 800 μm, which could be attributed to the difference of free carbon contents in the scaffolds with different spacing of adjacent fibers at the same size. To form larnite phase through the reaction between silicone resin and $CaCO_3$ fillers, it is necessary to keep the stoichiometric Ca/Si ratio of 2:1 in this study. Thus, the close contents of carbon atoms were pyrolyzed to form free carbons in the larnite/C scaffolds though the pyrolyzed temperature increased from 1000 °C to 1200 °C.

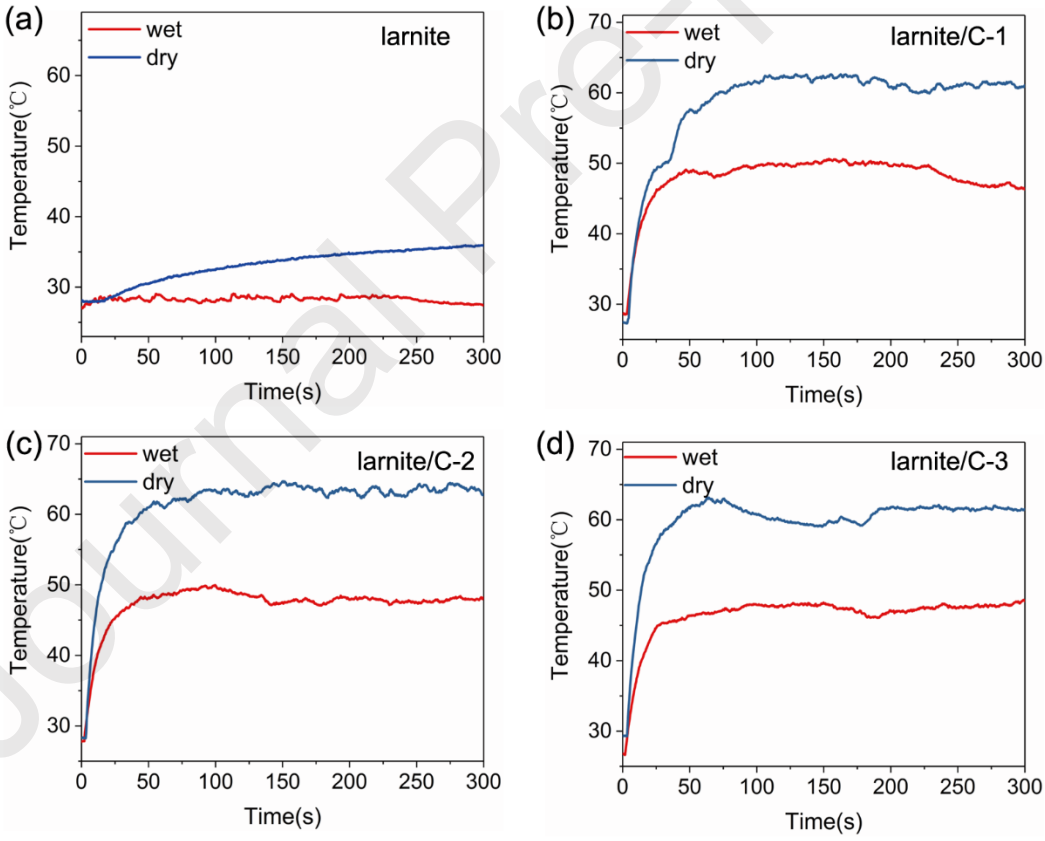

Fig. 3 In vitro photothermal effect of the larnite and larnite/C scaffolds at a power intensity of 0.75 W/cm^2 for 5 min. (a) larnite, (b) larnite/C-1, (c) larnite/C-2 and (d) larnite/C-3 in dry and wet (in PBS) conditions.

To determine if the photothermal effect of fabricated scaffolds is efficient for in vivo tumor ablation, the larnite and larnite/C scaffolds were further implanted into tumor-bearing nude mice. As shown in Fig. 4, the temperature at the location of the implanted larnite/C-3 scaffolds increased to 46 ^{o}C after NIR light irradiation (0.75 W/cm^2), which is in the temperature range of hyperthermia therapy. On the other hand, increasing the NIR light power intensity to 1.0 W/cm^2, the temperature could increase to 68 ^{o}C in 10 min. When the NIR light irradiation stopped, the temperature could decrease rapidly to the initial temperature. By contrast, the larnite scaffolds could not generate enough heat to achieve the hyperthermia temperature. Therefore, the larnite/C scaffolds showed great potential to treat tumors with photothermal therapy.

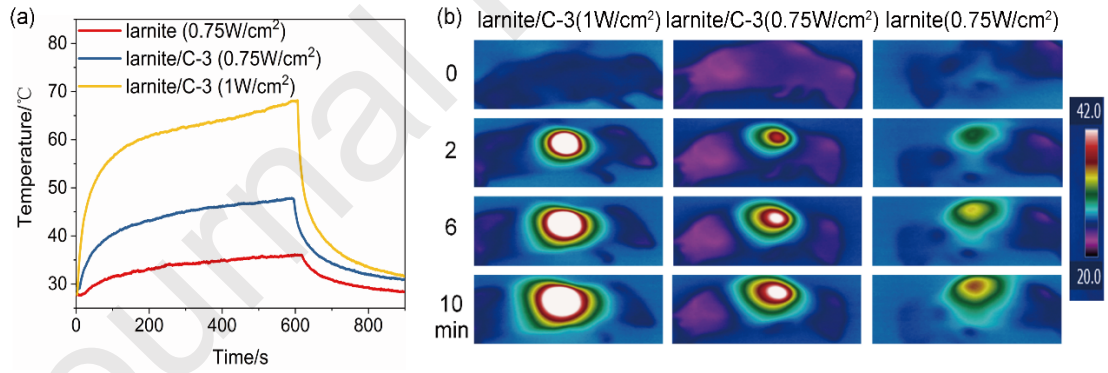

Fig. 4 In vivo photothermal effect of the larnite and larnite/C scaffolds. (a) Heating curves of the larnite and larnite/C-3 scaffolds with 808 laser irradiation in nude mice, and (b) their corresponding infrared thermal images.

The photothermal effect of the larnite/C scaffolds for killing tumor cells was evaluated by in vitro and in vivo. The viability of osteosarcoma cells (MNNG/HOS)

cultured on larnite/C-3 scaffolds was determined by CCK-8 assay and was shown in Fig. 5(a), and it is clear to see that the cell viability decreased with the increase of NIR light power intensity. Compared to the control group, the cell viabilities were 70±5 %, 48±4 %, 27±3 % and 5±2 % for those cases with a power intensity of 0.5 W/cm^2, 0.75 W/cm^2, 1 W/cm^2 and 1.25 W/cm^2, respectively. Fig. 5(b) showed fluorescent images of osteosarcoma cells (MNNG/HOS) stained with calcein AM (live cells, green fluorescence) and PI (dead cells, red fluorescence) for the scaffolds with or without NIR light irradiation. For pure larnite scaffolds, MNNG/HOS cells showed green fluorescence and little red fluorescence could be observed with and without NIR light irradiation, suggesting that pure larnite scaffolds had good biocompatibility, but poor photothermal effect. On the other hand, for the larnite/C-3 scaffolds, MNNG/HOS cells show green fluorescence without NIR light irriadiation, but most of MNNG/HOS cells present red fluorescence with NIR light irradiation. It indicated that the larnite/C-3 scaffolds exhibited excellent photothermal effect for killing tumor cells with NIR light irradiation. Here, the regional hyperthermia effect caused the death of MNNG/HOS cells.

The photothermal effect of the larnite/C-3 scaffolds in vivo therapy was shown in Fig. 5(c-e). After a 14-day photothermal treatment, the tumor volume in the larnite/C-3 scaffold group with NIR light irradiation decreased significantly, compared to the larnite scaffold group and the larnite/C-3 scaffold group without NIR light irradiation. Furthermore, the photothermal effect of the larnite/C-3 scaffolds was still excellent after implanting in mice for 14 days (Fig.5 (d)). It indicated that the larnite/C

scaffolds are possible for longer photothermal therapy, which could be attributed to the slow degradation of the larnite/C scaffolds. Furthermore, hematoxylin and eosin (H&E) staining results of the larnite/C scaffolds treated osteosarcoma indicated the significant necrosis of tumor tissue as shown in Fig. 5(e). The nucleus of tumor cells disappeared obviously in the larnite/C-3 scaffold group with NIR light irradiation, while there were a large number of tumor cell nucleus in other three groups. These results indicated that the larnite/C-3 scaffolds with NIR light irradiation show excellent photothermal therapy ability in vivo.

Larnite and free carbon are two components in the larnite/C scaffolds, and it has been proved that the significant photothermal effect is attributed to the existence of free carbons instead of larnite (Fig. 3 and Fig. 4). The photothermal effect refers to the temperature increase by NIR light irradiation, which is caused by the interaction between photon energy and the lattice. Carbon is a common photothermal agent, and has a high photothermal conversion efficiency to kill tumor cells and inhibit tumor growth. In this study, the temperature increase (46 ^{o}C) with holding time can kill tumor cells and inhibit tumor growth, which could be attributed to the irreversible protein denaturation and cell membrane damage, as well as late progressive apoptosis [20, 21], and Melamed et al. [47] discussed that the tumor cell death by photothermal therapy is depended on the intrinsic apoptosis pathway. On the other hand, the vessel distribution in tumor tissue is disorder, which prejudices heat dissipation, resulting in a poorer heat-resisting ability than normal tissues. However, there are few researches on the fundamental mechanisms underlying cell death by photothermal effect.

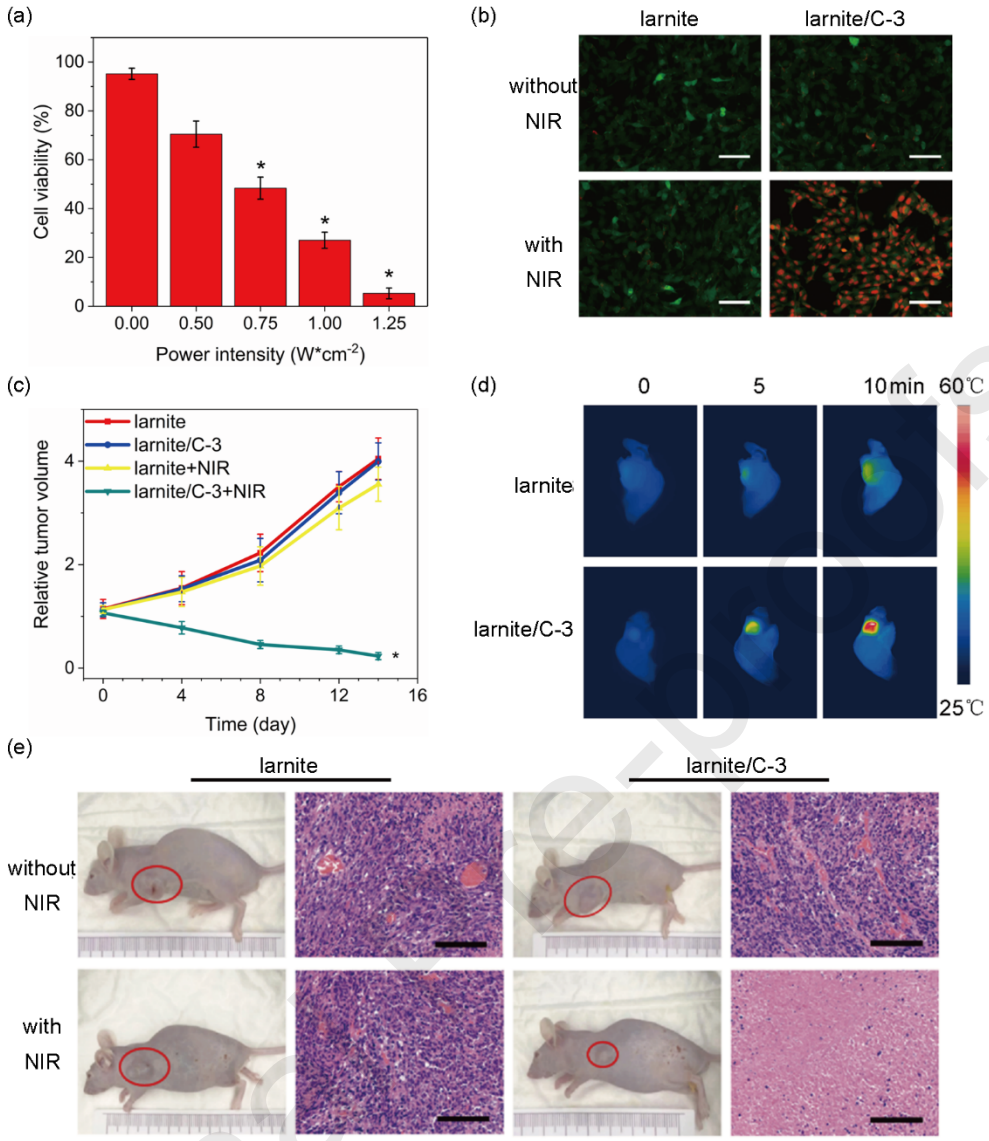

Fig. 5 In vitro and vivo evaluation of the larnite/C scaffolds for killing tumor cells and inhibiting tumor growth. (a) Cell viabilities of MNNG/HOS cells at different NIR light power intensities. (b) Fluorescent images of MNNG/HOS cells stained with calcein AM (live cells, green fluorescence) and PI (dead cells, red fluorescence) for the larnite and larnite/C-3 scaffolds (scale bar: 100 μm). (c) Time-dependent tumor growth curves of the mice with tumors using different treatments. (d) Infrared thermal images of the nude mice irradiated by 808 nm laser (0.75 W/cm^2) at day 14. (e) Optical photographs of the mice with tumors with different treatments and the corresponding H&E stained

images of MNNG tumor tissue on day 14 (scale bar: 100 μm). (* indicated significant difference, $p < 0.05$)

The high osteogenic capability of larnite/C scaffolds was also demonstrated both in vitro and in vivo. The adhesion of rat bone mesenchymal stem cells (rBMSCs) on the larnite and larnite/C-3 scaffolds were visualized by CLSM (Fig. 6(a)). A dense layer of rBMSCs spread and grow on the surface of larnite and larnite/C-3 scaffolds uniformly on day 3, featuring phenotype characteristics of the healthy striation of the cytoskeleton, which demonstrated that an interconnected and hierarchical porous structure of fabricated scaffolds is favorable for cell infiltration and proliferation in a 3D-penetrating microenvironment. Quantitative measurement using a CCK-8 assay showed an increase in the number of cells with culture time for both groups of scaffolds (Fig. 6(b)). There was no significant difference between the two groups, which indicated that free carbon-embedding scaffolds were not toxic to the rBMSCs. Similar to the cell proliferation results, the ALP activity and staining assay showed an increase with culture time for both larnite and larnite/C-3 scaffolds, but there was no significant difference between the two groups (Fig. 6(c)). In addition, extracellular matrix mineralization of the scaffolds were evaluated by alizarin red staining on day 7 and 14 (Fig. 6(d)). Both pure larnite and larnite/C-3 scaffolds produced mineralized nodules (red), but the larnite/C-3 scaffolds exhibited more mineralized nodules, suggesting higher calcium content of rBMSCs cultured on the larnite/C-3 scaffolds and better mineralization ability of the larnite/C-3 scaffolds. Cell differentiation of rBMSCs

on larnite and larnite/C-3 scaffolds was further evaluated by osteogenic expression determined by the expressions of osteogenic markers ALP, OCN and Runx-2 at 7 and 14 days (Fig. 6(e)). The osteogenic-related gene expression of rBMSCs was upregulated on larnite/C-3 scaffolds compared to pure larnite after 14 days ($P < 0.05$), indicating that free carbon embedding into the larnite scaffolds could promote osteogenic differentiation.

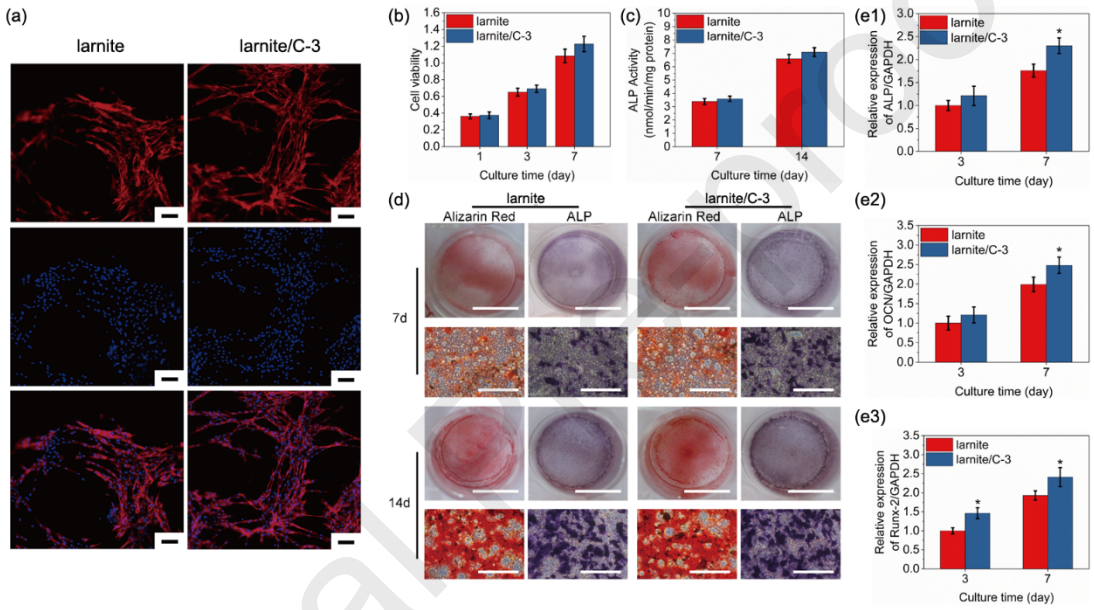

Fig. 6 In vitro cellular response of the larnite and larnite/C scaffolds. (a) LSCM image of rBMSCs seeded on larnite and larnite/C-3 scaffold. Cell nuclei and cytoskeleton of rBMSCs were stained with DAPI and rhodamine phalloidin (scale bar 10 μm) (b) Quantitative analysis of the proliferation of rBMSCs cultured on the scaffolds for 1, 3 and 7 days (n= 3). (c) ALP activity of rBMSCs cultured on the scaffolds for 7 and 14 days (n= 3). (d) ECM mineralization (red) and ALP (blue) staining of rBMSCs cultured on the scaffolds (scale bar: 7.5 mm and 100 μm). The osteogenesis-related gene expression of (e1) ALP, (e2) OCN and (e3) Runx-2 for rBMSCs cultured on the scaffolds by qRT-PCR analysis for 3 and 7 days (n= 3). (* indicated significant difference, $p < 0.05$)

Fig. 7 showed the in vivo osteogenesis performance of the larnite and larnite/C-3 scaffolds. Reconstructed micro-CT images showed a greater amount of new bone in the defects implanted with the larnite/C-3 scaffolds than in the defects implanted with the larnite scaffolds (Fig. 7(a), top and bottom views). Gaps were also evident at the periphery of the larnite implants and the host bone, and new bone formation in the defects implanted with the larnite/C-3 scaffolds appeared to be greater than in the defects implanted with the larnite scaffolds (Fig. 7(a)). In detail, the new bone mineral density (BMD) of the larnite/C-3 scaffolds (0.41 g/cm^3) was higher than that of the larnite scaffolds (0.3 g/cm^3), and the larnite/C-3 scaffolds showed higher bone volume/tissue volume (BV/TV) ratio (40 %) compared to the larnite scaffolds (35 %). The process of new bone formation was evaluated histomorphometrically by fluorochrome labeling at successive intervals of 2, 4 and 6 weeks with tetracycline, alizarin red and calcein fluorescence, respectively (Fig. 7(d)). It can be observed that the percent of all yellow, green and red fluorescence labeling in the larnite/C-3 scaffolds was significantly greater than in the larnite scaffolds, suggesting better new bone formation ability of the larnite/C-3 scaffolds. On the other hand, from histological analysis stained by H&E and Masson (Fig. 7(e)), much more newly formed bone could be observed in the larnite/C-3 scaffold group compared to the larnite scaffold group. Immunohistochemical analysis showed limited positive staining for OCN (a late osteogenic marker) and Runx-2 in the defects implanted with the larnite scaffolds and a greater amount of positive staining in the defects implanted with the

larnite/C-3 scaffolds at 8 weeks post-implantation. Taken together, these results showed that the larnite/C-3 scaffolds had a greater capacity to regenerate bone in rat calvarial defects when compared to pure larnite scaffolds.

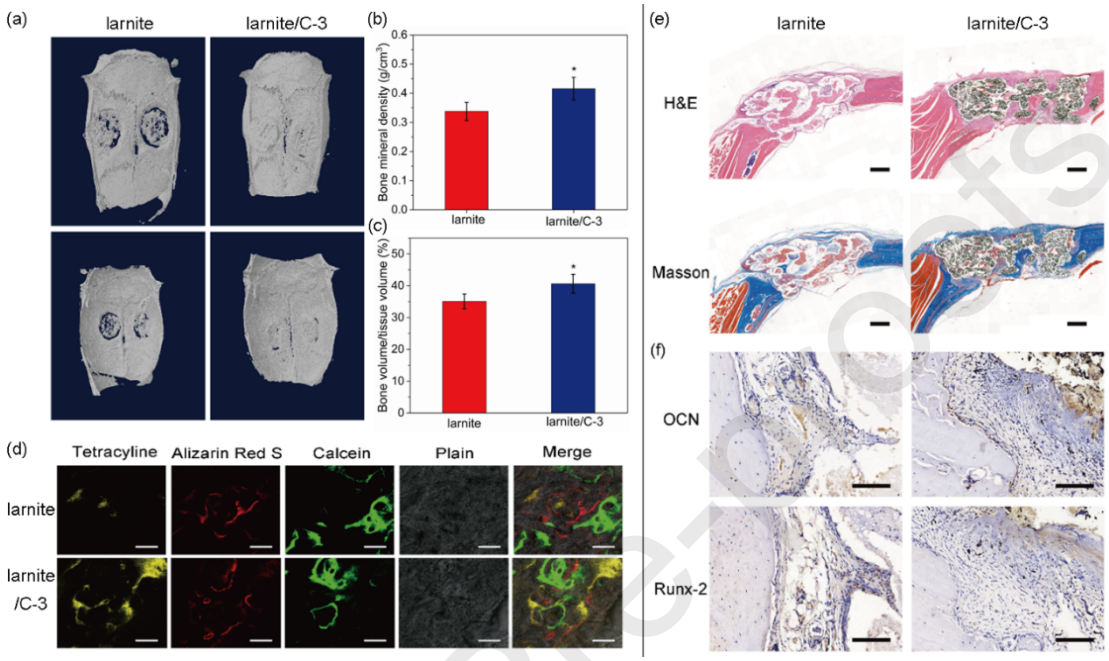

Fig. 7 In vivo osteogenesis performance of the larnite/C scaffolds. (a) 3D reconstruction of micro-CT images. (b) BMD and (c) BV/TV for the larnite and larnite/C-3 groups. (d) New bone formation and mineralization determined histomorphometrically by fluorochrome-labeling analysis. Yellow represents tetracycline at week 2, red represents alizarin red at week 4, green represents calcein at week 6 (scale bar: 100 μm). (e) Histological analysis stained by H&E and Masson (scale bar: 500 μm,). (f) Immunohistochemical staining evaluation of OCN and Runx-2 proteins (scale bar: 100 μm). (* indicated significant difference, $p < 0.05$)

In this study, the larnite/C scaffolds enhanced photothermal effect, because the free carbons in the scaffolds can adsorb NIR light and convert to thermal energy,

resulting in a temperature increase for the scaffolds. The results showed that the photothermal effect was weakened in a wet condition and in vivo (Fig. 3 and Fig. 4), which could be attributed to the transferring of the generated heat to the surrounding environment. However, the temperature increase in vivo satisfied the hyperthermia therapy, and could also be easily adjusted by changing the laser power intensity, which could meet the requirements of killing tumor cells. Thus, the larnite/C scaffolds have great potential for treating bone tumors.

By comparing the photothermal effects *in vivo* at day 0 (Fig. 4) with that at day 14 (Fig. 5(d)), it could be observed that the dissipating heat region abated over time. On the other hand, the scaffolds became incomplete compared to the original shape according to the results in micro-CT (Fig. 7(a)). Hence, larnite/C and larnite scaffolds were biodegradable. Calcium (Ca) and silicon (Si) are two main elements in larnite scaffolds, and are able to gradually dissolve into solution in a form of ions from the scaffolds. On the other hand, some important signaling pathways including Wnt/β-catenin, Notch, BMP/TGF-β, PI3K/Akt/mTOR, mitogen-activated protein kinase (MAPK), PDGF, IGF, FGF, Ca^{2+} pathways, etc. have been revealed and affect bone formation [48], and the dissolved calcium and silicon ions could stimulate some of them. For instance, Zhai et al. [49] proved that nagelschmidtite ($Ca_7P_2Si_2O_{16}$) silicate bioceramic could stimulate BMP signaling pathway of osteoblast MC3T3-E1 for new bone formation. Han et al. [50] demonstrated lithium ions incorporated mesoporous bioactive glass (Li-MBG) promoted new bone formation via the activation of Wnt/β-catenin signaling pathway. Afterwards, free carbons in larnite scaffolds further

enhanced osteogenic level according to the results in Fig. 6 and Fig. 7, and carbon is helpful in the process of cell differentiation of new bone formation. Shao et al. and Khajuria et al. [33, 51] proved that carbon dots were able to augment osteogenic differentiation, because carbon dots could upregulate the expression of Runx-2, ALP, OCN and BSP as well as extracellular matrix mineralization. The same phenomenon could be observed in this study, and the osteogenesis-related gene expression such as OCN, ALP and Runx-2 was also upregulated by free carbons in the larnite/C-3 scaffolds. As known, OCN is a non-collagenous protein of the bone extracellular-matrix in the process of bone formation, which has a high affinity for calcium ions, and Runx-2 is a member of Runt domain family of transcription factors, which is one of the most powerful molecular determinants of osteoblast differentiation. Therefore, new bone formation could be attributed to the synergies between osteoblast differentiation and proteins operation, and the free carbons promoted the new bone forming ability of the larnite/C scaffolds, which is promising for bone generation.

In this study, the nude mice with tumor and the Sprague Dawley rats with calvarial defects were employed for evaluating the potentials on treating bone tumors and bone regeneration, respectively. Tumor-bearing nude mice model is the most common tumor model currently available. For example, Yang et al. [26] designed a nude mice with tumor in the neck and Sprague-Dawley rats with calvarias defects model to evaluate the scaffolds of tumor treatment and bone regeneration abilities, and the similar model was constructed by Dang et al. [25] and Ma et al. [21, 52]. However, for osteosarcomatous research, larger animal models (such as larger rats or

rabbits) should be used to offer a relatively large bone defects to evaluate the osteogenic capability of scaffolds. To the best of our knowledge, there are no studies have successfully established an osteosarcomatous model in such larger animals to evaluate the therapeutic outcome of tumor ablation and bone regeneration simultaneously due to the intrinsic immunological rejection. Therefore, on account of the difficulties to develop osteosarcoma in the same in vivo model, the photothermal therapeutic efficacy and osteogenic potential of larnite/C scaffolds were evaluated separately in this study. It also can be believed that two animal models are proper to evaluate the abilities of larnite/C scaffolds with anti-tumor treatment and bone regeneration.

4. Conclusion

In summary, the free carbon-embedding larnite scaffolds were successfully derived from a preceramic resin and active fillers by 3D printing and ceramic transformation under an inert atmosphere. The obtained larnite/C scaffolds showed excellent photothermal effect to kill bone tumor cells in vitro and in vivo. Moreover, the larnite/C scaffolds promoted cell differentiation and possessed better bone regeneration ability compared to the pure larnite scaffolds. Therefore, this study provide a novel strategy to fabricate multifunctional bioceramic scaffolds for treating the tumor-related bone defects.

Acknowledgment

The authors gratefully acknowledge the support by grants from the National Natural Science Foundation of China (No. 51872185, 51972212 and 81601886), the Science and Technology Commission of Shanghai Municipality (NO. 17060502400), and the University of Shanghai for Science and Technology (No. 2018KJFZ016 and 2019KJFZ023).

References

[1] P. Pei, X. Qi, X. Du, M. Zhu, S. Zhao, Y. Zhu, Three-dimensional printing of tricalcium silicate/mesoporous bioactive glass cement scaffolds for bone regeneration, J. Mater. Chem. B 4 (2016) 7452-7463.

[2] X. Du, B. Yu, P. Pei, H. Ding, B. Yu, Y. Zhu, 3D printing of pearl/$CaSO_4$ composite scaffolds for bone regeneration, J. Mater. Chem. B 6 (2018) 499-509.

[3] J. Zhang, S. Zhao, Y. Zhu, Y. Huang, M. Zhu, C. Tao, C. Zhang, Three-dimensional printing of strontium-containing mesoporous bioactive glass scaffolds for bone regeneration, Acta Biomater. 10 (2014) 2269-2281.

[4] I. Pires, B. Gouveia, J. Rodrigues, R. Fonte, Characterization of sintered hydroxyapatite samples produced by 3D printing, Rapid Prototyp. J. 20 (2014) 413-421.

[5] H. Seitz, W. Rieder, S. Irsen, B. Leukers, C. Tille, Three-dimensional printing of porous ceramic scaffolds for bone tissue engineering, J. Biomed. Mater. Res. B Appl. Biomater. 74 (2005) 782-788.

[6] K.C. Kolan, M.C. Leu, G.E. Hilmas, R.F. Brown, M. Velez, Fabrication of 13-93

bioactive glass scaffolds for bone tissue engineering using indirect selective laser sintering, Biofabrication 3 (2011) 025004.

[7] P. Pei, Z. Tian, Y. Zhu, 3D printed mesoporous bioactive glass/metal-organic framework scaffolds with antitubercular drug delivery, Micropor. Mesopor. Mater. 272 (2018) 24-30.

[8] E. Vorndran, M. Klarner, U. Klammert, L.M. Grover, S. Patel, J.E. Barralet, U. Gbureck, 3D powder printing of β-tricalcium phosphate ceramics using different strategies, Adv. Eng. Mater. 10 (2008) B67-B71.

[9] T. Almela, I.M. Brook, K. Khoshroo, M. Rasoulianboroujeni, F. Fahimipour, M. Tahriri, E. Dashtimoghadam, A. El-Awa, L. Tayebi, K. Moharamzadeh, Simulation of cortico-cancellous bone structure by 3D printing of bilayer calcium phosphate-based scaffolds, Bioprinting 6 (2017) 1-7.

[10] X. Du, S. Fu, Y. Zhu, 3D printing of ceramic-based scaffolds for bone tissue engineering: an overview, J. Mater. Chem. B 6 (2018) 4397-4412.

[11] A. Butscher, M. Bohner, C. Roth, A. Ernstberger, R. Heuberger, N. Doebelin, P.R. von Rohr, R. Muller, Printability of calcium phosphate powders for three-dimensional printing of tissue engineering scaffolds, Acta Biomater. 8 (2012) 373-385.

[12] S.-Y. Fu, B. Yu, H.-F. Ding, G.-D. Shi, Y.-F. Zhu, Zirconia-incorporation in 3D printed β-Ca_2SiO_4 scaffolds on their physicochemical and biological properties, J. Inorg. Mater. 34 (2019) 444-454.

[13] Z. Wang, P. Huang, O. Jacobson, Z. Wang, Y. Liu, L. Lin, J. Lin, N. Lu, H. Zhang, R. Tian, G. Niu, G. Liu, X. Chen, Biomineralization-inspired synthesis of copper sulfide-

ferritin nanocages as cancer theranostics, ACS Nano 10 (2016) 3453-3460.

[14] H. Liu, D. Chen, L. Li, T. Liu, L. Tan, X. Wu, F. Tang, Multifunctional gold nanoshells on silica nanorattles: a platform for the combination of photothermal therapy and chemotherapy with low systemic toxicity, Angew Chem. Int. Ed. Engl. 50 (2011) 891-895.

[15] Y. Yang, J. Liu, C. Liang, L. Feng, T. Fu, Z. Dong, Y. Chao, Y. Li, G. Lu, M. Chen, Z. Liu, Nanoscale metal-organic particles with rapid clearance for magnetic resonance imaging-guided photothermal therapy, ACS Nano 10 (2016) 2774-2781.

[16] L. Cheng, W. He, H. Gong, C. Wang, Q. Chen, Z. Cheng, Z. Liu, PEGylated micelle nanoparticles encapsulating a non-fluorescent near-infrared organic dye as a safe and highly-effective photothermal agent for in vivo cancer therapy, Adv. Funct. Mater. 23 (2013) 5893-5902.

[17] J.T. Robinson, S.M. Tabakman, Y. Liang, H. Wang, H.S. Casalongue, D. Vinh, H. Dai, Ultrasmall reduced graphene oxide with high near-infrared absorbance for photothermal therapy, J. Am. Chem. Soc. 133 (2011) 6825-6831.

[18] K. Yang, H. Xu, L. Cheng, C. Sun, J. Wang, Z. Liu, In vitro and in vivo near-infrared photothermal therapy of cancer using polypyrrole organic nanoparticles, Adv. Mater. 24 (2012) 5586-5592.

[19] X. Huang, M.A. El-Sayed, Gold nanoparticles: Optical properties and implementations in cancer diagnosis and photothermal therapy, J. Adv. Res. 1 (2010) 13-28.

[20] X. Wang, T. Li, H. Ma, D. Zhai, C. Jiang, J. Chang, J. Wang, C. Wu, A 3D-printed

scaffold with MoS_2 nanosheets for tumor therapy and tissue regeneration, NPG Asia Mater. 9 (2017) e376.

[21] H. Ma, C. Jiang, D. Zhai, Y. Luo, Y. Chen, F. Lv, Z. Yi, Y. Deng, J. Wang, J. Chang, C. Wu, A Bifunctional biomaterial with photothermal effect for tumor therapy and bone regeneration, Adv. Funct. Mater. 26 (2016) 1197-1208.

[22] M. Zheng, Y. Li, S. Liu, W. Wang, Z. Xie, X. Jing, One-Pot to synthesize multifunctional carbon dots for near infrared fluorescence imaging and photothermal cancer therapy, ACS Appl. Mater. Interfaces 8 (2016) 23533-23541.

[23] J. Ge, Q. Jia, W. Liu, M. Lan, B. Zhou, L. Guo, H. Zhou, H. Zhang, Y. Wang, Y. Gu, X. Meng, P. Wang, carbon dots with intrinsic theranostic properties for bioimaging, red-light-triggered photodynamic/photothermal simultaneous therapy in vitro and in vivo, Adv. Healthc. Mater. 5 (2016) 665-675.

[24] X. Yao, X. Niu, K. Ma, P. Huang, J. Grothe, S. Kaskel, Y. Zhu, Graphene quantum dots-capped magnetic mesoporous silica nanoparticles as a multifunctional platform for controlled drug delivery, magnetic hyperthermia, and photothermal therapy, Small 13 (2017) 1602225.

[25] W. Dang, T. Li, B. Li, H. Ma, D. Zhai, X. Wang, J. Chang, Y. Xiao, J. Wang, C. Wu, A bifunctional scaffold with $CuFeSe_2$ nanocrystals for tumor therapy and bone reconstruction, Biomaterials 160 (2018) 92-106.

[26] B. Yang, J. Yin, Y. Chen, S. Pan, H. Yao, Y. Gao, J. Shi, 2D-black-phosphorus-reinforced 3d-printed scaffolds: a stepwise countermeasure for osteosarcoma, Adv. Mater. 30 (2018) 1705611.

[27] Z.C. Eckel, C. Zhou, J.H. Martin, A.J. Jacobsen, W.B. Carter, T.A. Schaedler, Additive manufacturing of polymer-derived ceramics, Science 351 (2016) 58-62.

[28] A. Zocca, G. Franchin, H. Elsayed, E. Gioffredi, E. Bernardo, P. Colombo, Direct ink writing of a preceramic polymer and fillers to produce hardystonite ($Ca_2ZnSi_2O_7$) bioceramic scaffolds, J. Am. Ceram. Soc. 99 (2016) 1960-1967.

[29] H. Elsayed, P. Colombo, E. Bernardo, Direct ink writing of wollastonite-diopside glass-ceramic scaffolds from a silicone resin and engineered fillers, J. Eur. Ceram. Soc. 37 (2017) 4187-4195.

[30] A. Zocca, H. Elsayed, E. Bernardo, C.M. Gomes, M.A. Lopez-Heredia, C. Knabe, P. Colombo, J. Gunster, 3D-printed silicate porous bioceramics using a non-sacrificial preceramic polymer binder, Biofabrication 7 (2015) 025008.

[31] L. Fiocco, S. Agnoli, D. Pedron, M. Secco, S. Tamburini, L. Ferroni, C. Gardin, B. Zavan, E. Bernardo, Wollastonite-diopside-carbon composite foams from a silicone resin and inorganic fillers, Ceram. Int. 44 (2018) 931-937.

[32] H. Elsayed, F. Carraro, S. Agnoli, D. Bellucci, V. Cannillo, L. Ferroni, C. Gardin, B. Zavan, E. Bernardo, Direct ink writing of silica-carbon-calcite composite scaffolds from a silicone resin and fillers, J. Eur. Ceram. Soc. 38 (2018) 5200-5207.

[33] D. Shao, M. Lu, D. Xu, X. Zheng, Y. Pan, Y. Song, J. Xu, M. Li, M. Zhang, J. Li, G. Chi, L. Chen, B. Yang, Carbon dots for tracking and promoting the osteogenic differentiation of mesenchymal stem cells, Biomater. Sci. 5 (2017) 1820-1827.

[34] Z. Gou, J. Chang, W. Zhai, Preparation and characterization of novel bioactive dicalcium silicate ceramics, J. Eur. Ceram. Soc. 25 (2005) 1507-1514.

[35] S. Fu, W. Liu, S. Liu, S. Zhao, Y. Zhu, 3D printed porous β-Ca_2SiO_4 scaffolds derived precermic resin and their physicochemical and biological propeerties, Sci. Technol. Adv. Mater. 19 (2018) 495-506.

[36] Z. Gou, J. Chang, W. Zhai, J. Wang, Study on the self-setting property and the in vitro bioactivity of beta-Ca_2SiO_4, J. Biomed. Mater. Res. B Appl. Biomater. 73 (2005) 244-251.

[37] Y. Dai, H. Liu, B. Liu, Z. Wang, Y. Li, G. Zhou, Porous β-Ca_2SiO_4 ceramic scaffolds for bone tissue engineering: In vitro and in vivo characterization, Ceram. Int. 41 (2015) 5894-5902.

[38] L. Cao, X. Wang, M.J. Meziani, F. Lu, H. Wang, P.G. Luo, Y. Lin, B.A. Harruff, L.M. Veca, D. Murray, S.Y. Xie, Y.P. Sun, Carbon dots for multiphoton bioimaging, J. Am. Chem. Soc. 129 (2007) 11318-11319.

[39] S.-T. Yang, L. Cao, P.G. Luo, F. Lu, X. Wang, H. Wang, M.J. Mezian, Y. Liu, G. Qi, Y.-P. Sun, Carbon dots for optical imaging in vivo, J. Am. Chem. Soc. 131 (2009) 11308–11309.

[40] L. Cao, S. Sahu, P. Anilkumar, C.E. Bunker, J. Xu, K.A. Fernando, P. Wang, E.A. Guliants, K.N. Tackett, 2nd, Y.P. Sun, Carbon nanoparticles as visible-light photocatalysts for efficient CO_2 conversion and beyond, J. Am. Chem. Soc. 133 (2011) 4754-4757.

[41] L. Zhou, Y. Lin, Z. Huang, J. Ren, X. Qu, Carbon nanodots as fluorescence probes for rapid, sensitive, and label-free detection of Hg^{2+} and biothiols in complex matrices, Chem. Commun. 48 (2012) 1147-1149.

[42] W. Booncharoen, A. Jaroenworaluck, R. Stevens, A synthesis route to nanoparticle dicalcium silicate for biomaterials research, J. Biomed. Mater. Res. B 99 (2011) 230-238.

[43] D. Correa, A. Almirall, R. Garcia-Carrodeguas, L.A. dos Santos, A.H. De Aza, J. Parra, J.A. Delgado, beta-dicalcium silicate-based cement: synthesis, characterization and in vitro bioactivity and biocompatibility studies, J. Biomed. Mater. Res. A 102 (2014) 3693-3703.

[44] M. Yan, W. Song, C. Zhao-hui, Raman spectroscopy studies of the high-temperature evolution of the free carbon phase in polycarbosilane derived SiC ceramics, Ceram. Int. 36 (2010) 2455-2459.

[45] I. Gonzalo-Juan, R. Detsch, S. Mathur, E. Ionescu, A.R. Boccaccini, R. Riedel, Synthesis and in vitro activity assessment of novel silicon oxycarbide-based bioactive glasses, Materials 9 (2016) 959.

[46] L. Fiocco, H. Elsayed, D. Badocco, P. Pastore, D. Bellucci, V. Cannillo, R. Detsch, A.R. Boccaccini, E. Bernardo, Direct ink writing of silica-bonded calcite scaffolds from preceramic polymers and fillers, Biofabrication 9 (2017) 025012.

[47] J.R. Melamed, R.S. Edelstein, E.S. Day, Elucidating the fundamental mechanisms of cell death triggered by photothermal therapy, ACS Nano 9 (2015) 6-11.

[48] M. Majidinia, A. Sadeghpour, B. Yousefi, The roles of signaling pathways in bone repair and regeneration, J. Cell. Physiol. 233 (2018) 2937-2948.

[49] D. Zhai, M. Xu, L. Liu, J. Chang, C. Wu, Silicate-based bioceramics regulating osteoblast differentiation through a BMP_2 signalling pathway, J. Mater. Chem. B 5

(2017) 7297-7306.

[50] P. Han, C. Wu, J. Chang, Y. Xiao, The cementogenic differentiation of periodontal ligament cells via the activation of Wnt/beta-catenin signalling pathway by Li^+ ions released from bioactive scaffolds, Biomaterials 33 (2012) 6370-6379

[51] D.K. Khajuria, V.B. Kumar, D. Gigi, A. Gedanken, D. Karasik, Accelerated bone regeneration by nitrogen-doped carbon dots functionalized with hydroxyapatite nanoparticles, ACS Appl. Mater. Interfaces 10 (2018) 19373-19385.

[52] H. Ma, J. Luo, Z. Sun, L. Xia, M. Shi, M. Liu, J. Chang, C. Wu, 3D printing of biomaterials with mussel-inspired nanostructures for tumor therapy and tissue regeneration, Biomaterials 111 (2016) 138-148.

Research Highlights:

1. Free carbon-embedded larnite (larnite/C) scaffolds have been fabricated by 3D printing with preceramic-derived ceramics strategy.

2. Larnite/C scaffolds exhibit excellent photothermal effect and could inhibit the tumor growth.

3. Larnite/C scaffolds could stimulate new bone formation in critical-sized rat calvarial defects.